EXPLORING FLUIDIZED BED COMBUSTION FOR CARNOT BATTERIES BASED ON ZERO-CARBON IRON ENERGY CYCLES

Tomasz Wronski*[1], Francesco Murri[1,2], Adriano Sciacovelli*[1,3]

[1]University of Birmingham, School of Chemical Engineering, Birmingham, West Midlands, United Kingdom

[2]University of Pisa, Department of Energy, Systems, Territory and Construction Engineering, Italy

[3]University of Birmingham, Birmingham Energy Institute, Birmingham, West Midlands, United Kingdom

*Corresponding Authors: t.m.wronski@bham.ac.uk; a.sciacovelli@bham.ac.uk

ABSTRACT

Fluidized bed combustors are a potential alternative process for energy release in the zero-carbon iron-based energy cycle, characterized by subsequent metal oxide reduction and metal combustion. The study of the iron/iron oxide couple for clean energy storage has been favored compared to other reactive metals due to its preferred heterogeneous combustion mechanism. Recent advancements in fundamental knowledge on single iron particle combustion has allowed for the investigation of larger-scale combustion processes, focusing essentially on flames of pulverized, micrometric particles. Until now, these have shown significant nanoparticle production and poor combustion efficiency. In this study, fluidized bed processes are investigated as a promising alternative, especially because of the high heat transfer rates and temperature control they offer. First, analytical calculations provided initial flow and bed parameters suitable for fluidization and combustion of micrometric iron particles. Then, the Eulerian multiphase model coupled to a simplified combustion mechanism adapted from single-particle experimental data were implemented in the commercial software Fluent. Iron combustion was simulated under stoichiometric conditions in a small-scale fluidized bed with a 2 kW nominal heat output.

Our results highlight the conveniently similar fluidizing behavior of micrometric iron particles and iron oxide products. However, combustion simulations showed important inaccuracies regarding species balance, suggesting that a more accurate reaction model is needed before attempting a parametric analysis of the process. Overall, the study contributes to advance the understanding and development of a key component in zero-Carbon Iron Energy Cycles and associated potential implementation into a novel Carnot Battery technological solution.

1 INTRODUCTION

Reactive metals and their oxides have been proposed as potential zero-carbon energy carriers. This novel type of thermochemical energy storage relies on the virtuous energy cycle proposed by Bergthorson et al. (2015). Energy storage is achieved by reducing metal oxides using clean processes such as electrolysis (Allanore et al., 2011) or Direct Reduction of Iron with Hydrogen (DRIH) (Bhaskar et al., 2020; Julien & Bergthorson, 2017), and releasing it through metal combustion, which is a carbon-free reaction. Particularly when considering DRIH, the cycle utilizes the mature hydrogen electrolysis technology, but circumvents the unsolved issues regarding safe and efficient storage that arise for its use in direct combustion or fuel cells. Among other reactive metals, iron has been the focus of most research works due to its availability and preferred heterogeneous combustion reaction mechanism resulting in a lesser propensity to produce nanoparticles (Bergthorson, 2018). Recent experimental and numerical works on single, micrometric iron particle combustion (Ning et al., 2021, 2022; Thijs et al., 2022) significantly improved the understanding of the reaction mechanisms and encouraged the investigation of iron dust flames as an energy generation process (Baigmohammadi et al., 2023; Fedoryk et al., 2023; Mich et al., 2023). Fluidized bed combustion processes, on the other hand, have been largely ignored despite their significant usage for energy generation applications using other solid fuels such as coal or biomass. Nevertheless, fluidized bed processes usually present high heat transfer

https://doi.org/10.52202/077185-0084

rates, temperature control and fuel residence times (Sarkar, 2015), which could potentially address some of the problems that are yet to be solved in iron flames, namely a low combustion efficiency and nanoparticle generation (partially) due to high flame temperatures. For these reasons, fluidized bed combustion of iron could be integrated into novel, large-scale Carnot batteries based on the iron energy cycle, particularly using micrometric iron particles. Unlike direct reduction of iron oxide using hydrogen (DRIH), where particle sintering is a significant challenge, fluidized bed combustion for iron effectively mitigates sintering due to the protective oxide layer around iron particles. Carnot batteries is a technological class comprising thermo-mechanical and/or thermo-chemical processes for large storage of energy (Vecchi et al., 2022). Charging process typically consists in a power-to-X process, for example power-to-heat, with heat stored in thermal energy storage components (TES). Conversely during discharge, heat previously stored is converted back to electricity through a dedicated conversion cycle. Interest in Carnot batteries arises from the possibility to store and deliver different forms of energy, chiefly electricity and power, and for longer duration compared to electrochemical storage (Vecchi & Sciacovelli, 2023). Interest has also recently arisen around Carnot batteries concepts which comprises intermediate thermo-chemical energy storage, and in particular metal-oxides, as proposed and investigated in (Guío-Pérez et al., 2023; Janicka et al., 2023; Vecchi & Sciacovelli, 2023). In this study Carnot battery presented in Figure 1 is considered. The charging phase consists of iron oxide reduction using green hydrogen produced through water electrolysis. Steam and surplus hydrogen are recirculated, while the reduced iron metal is used as fuel in the energy discharge process based on iron combustion in a fluidized bed. The high-quality heat produced on demand can be used directly or converted to electricity, while the iron oxide products are recovered and reused in the next charging cycle. Thus, this novel Carnot battery concept retains the original principle of power-to-heat-to-power conversion, but charging and discharging processes can be spatially and temporally decoupled thanks to the ease of storage and transport of both iron and iron oxide.

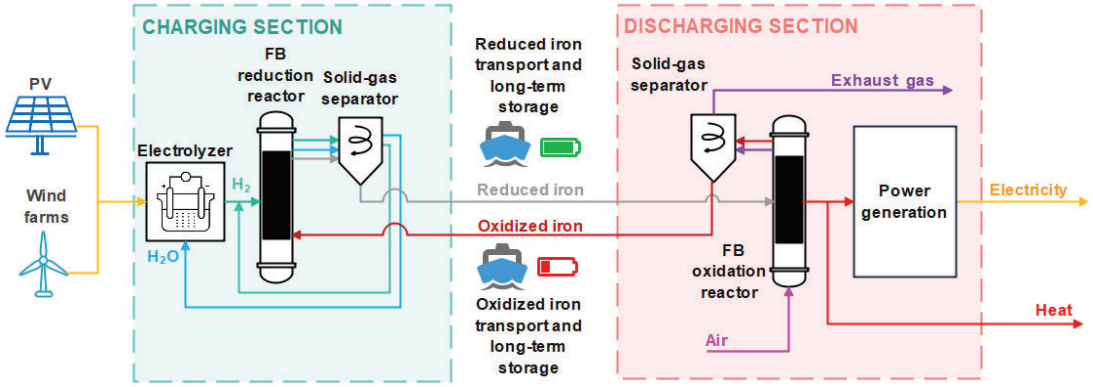

Figure 1: Process schematic of a novel Carnot battery based on DRIH and iron combustion in fluidized bed.

In the present study, we aim to provide a baseline for future experimental and numerical works on iron combustion in fluidized beds, thus focusing on the energy release part of the Carnot battery. To mitigate the absence of experimental data in this field, we used the extensive knowledge available on other fluidized bed processes, and particularly well-established correlations, to analytically estimate a baseline combination of particle size, bed temperature and fluidization velocity suitable for iron combustion. Following this analytical approach, we designed a small-scale, 3D CFD model on the commercial software ANSYS Fluent. Using the Eulerian multiphase model (two-fluid approach) and implementing a simplified combustion reaction mechanism adapted from single-particle experimental data, we simulated a small-scale fluidized bed combustor fueled by 100 µm iron particles and offering a heat output of 2 kW. The fluidization was modeled successfully and confirmed the suitability of the process for iron combustion. However, important inaccuracies regarding species conservation were observed, suggesting that a more complex reaction model is needed. Overall, this first attempt to assess the feasibility of fluidized bed processes for iron combustion provides a solid baseline and promising perspectives for future experimental and numerical works on the topic.

https://doi.org/10.52202/077185-0084

2 SYSTEM DESCRIPTION

For an initial assessment of the feasibility of fluidized bed iron combustion for energy release, simulating a simple, generic fluidized bed system was preferred. Additionally, a small scale was chosen that would more easily correspond to first experimental studies in the future. That includes a vertical cylindrical reactor, injectors for the fluidizing gas and iron particle fuel, and a gas outlet. The corresponding calculation domain for the CFD model is schematized in Figure 2 with dimensions determined through the zero-D analysis (section 4.1). The fluidizing gas is injected through the bottom inlet spreading through the entire cross-section of the cylinder. An additional circular inlet is located on the side wall, in the upper part of the reactor. This inlet allows the eventual injection of solid iron particles entrained in a nitrogen flow. A circular gas outlet is located at the top of the reactor. It is narrower than the reactor's diameter to induce an additional pressure drop and prevent the formation of a recirculation zone at the outlet. In all simulations, the oxide bed was initialized with a height of 3 cm and a volume fraction of 0.6 (corresponding to a settled bed).

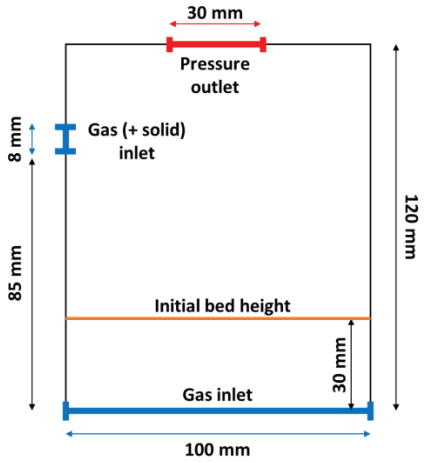

Figure 2: Schematic of the simulated system

3 METHODOLOGY

3.1 Characteristic velocities in fluidized bed systems

The target process in this study is a bubbling fluidized bed. It is therefore essential to determine the minimum fluidization velocity and terminal velocity for both iron and iron oxide particles, which will determine the gas velocity interval suitable for the process. The minimum velocity for fine particles can be approximated using the Wen and Yu equation (Kunii & Levenspiel, 2013):

$$u_{mf} = \frac{\mu}{d_s * \rho_g}\left[\left(33.7^2 + 0.0408\frac{d_s^3 \rho_g(\rho_s - \rho_g)g}{\mu^2}\right)^{\frac{1}{2}} - 33.7\right] \quad (1)$$

If the physical properties of the system are known, the terminal velocity of can be determined using the dimensionless particle size d_p* and dimensionless gas velocity $u*$, defined as follows:
These dimensionless variables are defined as follows:

$$d_p^* = d_p\left[\frac{\rho_g(\rho_s - \rho_g)g}{\mu^2}\right]^{1/3} \quad (2)$$

$$u^* = u\left[\frac{{\rho_g}^2}{\mu\,(\rho_s - \rho_g)g}\right]^{1/3} \quad (3)$$

For spherical particles, the dimensionless terminal velocity is then defined as

https://doi.org/10.52202/077185-0084

$$u_t^* = \left[\frac{18}{{d_p^*}^2} + \frac{0.591}{(d_p^*)^{0.5}}\right]^{-1} \tag{4}$$

These dimensionless variables are used in a modified Geldart chart (Kunii & Levenspiel, 2013) which extends its applicability to gases different than air and to non-atmospheric conditions. This is essential in the present study, where a bed temperature over 1100 K is considered, and provides an estimation of the particles behavior beyond what can be deduced from the critical velocities alone.

3.2 Eulerian multiphase model

Three-dimensional transient simulations of the fluidized bed combustion of iron are performed using the commercial software ANSYS Fluent V23.1. Second order discretization schemes were used for all equations and the time step was fixed at 0.0001 s. The Eulerian multiphase model was used, implying a Eulerian treatment of both gas and solid phases, which become interpenetrating continua. Instead of tracking each particle in time and space (Lagrangian approach), each phase is represented by its volume fraction. Continuity and momentum equations are solved for each phase q as follows (2023). Additionally, the Gidaspow drag model was also used (Gidaspow et al., 1991).

Continuity equation:

$$\frac{1}{\rho_{rq}}\left(\frac{\partial}{\partial t}(\alpha_q\rho_q) + \nabla.(\alpha_q\rho_q\vec{v}_q) = \sum_{p=1}^{n}\dot{m}_{pq}\right) \tag{5}$$

Momentum equation:

$$\frac{\partial}{\partial t}(\alpha_q\rho_q\vec{v}_q) + \nabla.(\alpha_q\rho_q\vec{v}_q\vec{v}_q) = -\alpha_q\nabla p + \nabla.\bar{\bar{\tau}}_q + \alpha_q\rho_q\vec{g} + \sum_{p=1}^{n}K_{pq}(\vec{v}_p - \vec{v}_q) + \dot{m}_{pq}\vec{v}_{pq} + \vec{F}_{td,q} \tag{6}$$

Energy equation:

$$\frac{\partial}{\partial t}\left(\alpha_q\rho_q\left(e_q + \frac{\vec{v}_q^2}{2}\right)\right) + \nabla\cdot\left(\alpha_q\rho_q\vec{v}_q\left(h_q + \frac{\vec{v}_q^2}{2}\right)\right) = \nabla\cdot\left(\alpha_q k_{eff,q}\nabla T_q - \sum_j h_{j,q}\vec{J}_{j,q} + \bar{\bar{\tau}}_{eff,q}\cdot\vec{v}_q\right) + \sum_{p=1}^{n}(Q_{pq} + \dot{m}_{pq}h_{pq}) + p\frac{\partial\alpha_q}{\partial t} + S_q \tag{7}$$

Chemical species conservation equation (the reaction rate R is defined in the following section):

$$\frac{\partial}{\partial t}(\rho^q\alpha^q Y_i^q) + \nabla\cdot(\rho^q\alpha^q\vec{v}^q Y_i^q) = -\nabla\cdot\alpha^q\vec{J}_i^q + R\cdot M_i \tag{8}$$

One of the shortcomings of the model is that an additional phase needs to be added for each different particle diameter. To reduce calculation time, the choice was made to model a monodisperse problem totaling 3 separate phases: the gas phase, the iron granular phase, and the iron oxide granular phase (both with a uniform particle size distribution).

3.3 Simplified reaction mechanism

Iron particle combustion has been studied extensively in the past. It was shown that the reaction mechanism varies significantly depending on experimental conditions, with both gas phase and surface reactions being possible(Sun et al., n.d.; Tang et al., 2011). In the context of zero-carbon energy release, gas phase combustion must be avoided, as it leads to both a material loss (which lowers the round-trip efficiency of the energy cycle) and nanoparticle formation (which represent a health and environmental hazard) (Ning et al., 2022; Thijs et al., 2022). Moreover, iron exists under different oxidized states. When a particle burns following the surface reaction mechanism, layers of different oxides develop on the particle, while the metallic iron core shrinks (Mi et al., 2022). In the context of an iron energy cycle, the final oxidation state Fe_2O_3 is preferred as its reduction process is more energy efficient than that of Fe_3O_4. The critical conditions ensuring a surface reaction as well as the production of Fe_2O_3 are still

https://doi.org/10.52202/077185-0084

being investigated; in this study, we will assume that no iron evaporates and that Fe_2O_3 is obtained following a simplified, single-step mechanism:

$$Fe + 1.5\ O_2 \rightarrow Fe_2O_3 \tag{9}$$

The reaction occurs for iron temperatures above 1080 K, which is the ignition temperature of micrometric iron particles in air (Mi et al., 2022). The reaction model is based on experimental data on single-particle combustion in air (Ning et al., 2021). In this study, Ning et al. link the particle burn time to its initial diameter as follows:

$$t_b = 0.000079 * d_p^{1.65} \tag{10}$$

This was used to determine an average reaction rate for a single particle with a diameter of 100 μm and adapted to a suspension of particles in a cell by including a dependency on the cell's iron volume fraction. The model reaction rate is therefore defined as follows:

$$R = A\left(\frac{\rho_{Fe}\alpha_{Fe}}{M_{Fe}}\right) \tag{11}$$

The proposed reaction rate is therefore very simplified, is independent of temperature and oxygen concentration, and is only valid for particles with an initial diameter of 100 micrometers. The present reaction model was first satisfactorily tested in a simplified case, where a homogeneous mixture of iron and air reacted in an enclosed box without any flow.

4 RESULTS AND DISCUSSION

4.1 Determination of baseline system parameters using analytical approach

In this study, the target system is a bubbling fluidized bed, which should provide the optimal conditions for iron particle combustion: high heat transfer rates, long residence time, and temperature stabilization through the high thermal inertia of the inert bed material. The first objective is to determine suitable conditions for fluidization and combustion of iron particles.

4.1.1 Bed temperature: Ignition temperature of iron particles (defined as the critical temperature over which the energy released by the oxidation reaction leads to thermal runaway) has been measured at approximately 1080 K for isolated micrometric (< 10 μm) particles (Mi et al., 2022). To avoid iron evaporation and subsequent nanoparticle formation, the temperature of the particles (and thus, that of the bed) should be kept at a minimum. In this study, an initial bed temperature of 1100 K was chosen.

4.1.2 Fluidizing gas velocity and particle size: Minimum fluidization and terminal velocities (Equations 1 - 4) were calculated for different diameters of spherical iron particles in air at 1100 K. These critical velocities were also calculated for corresponding iron oxide particle diameters, assuming complete combustion and zero material loss or porosity. The results are displayed in Figure 3.

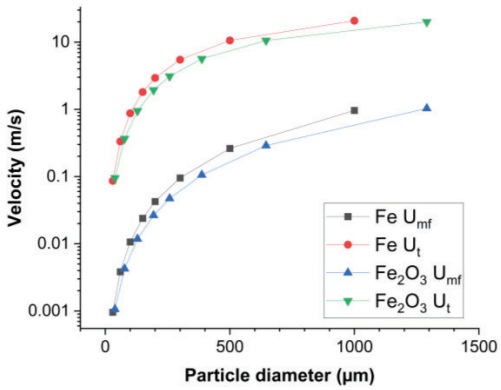

Figure 3: Minimum fluidization and terminal velocities for different iron and iron oxide particle diameters.

https://doi.org/10.52202/077185-0084

A very important observation is that despite the mass and size increase through the combustion reaction, iron particles and corresponding reacted iron oxide particles seem to have very similar minimum fluidization and terminal velocities. As such, the inert bed material can be exclusively composed of iron oxide particle products, without the need for sand or other material that would otherwise need to be separated from the products in the process, as is the case in coal combustion for example. The similarity of fluidization behavior of iron and oxide particles should also allow for very homogeneous iron and oxide particle distribution within the bed, thus optimizing the heat distribution and further reducing the probability of iron-iron contact and sintering of particles. Figure 3 also displays a clear area between the curves of u_{mf} and u_t corresponding to process conditions that would ensure no entrainment of reactant or product particles. However, in practice, fluidization does not only depend on those two critical velocities. The modified Geldart chart displayed in Figure 4 shows different regions of fluidizing behavior depending on the dimensionless variables d_p^* and u^*, and corrects some assumptions that could be made based on Figure 3 alone. For example, both Figure 3 and Figure 4 predict a terminal velocity of ~1 m/s for 100 µm iron particles (and 130 µm oxide particles), but the modified Geldart chart shows that bubbling fluidization can be expected for velocities well beyond that terminal velocity. This is due to gas bubbles rapidly passing through the bed without actually entraining particles. Another important piece of information is the Geldart class corresponding to the different particle sizes at such high temperatures. Satisfactory fluidization is usually only achieved for Geldart A (aeratable) and B (bubbling) classes. For the present conditions (1100 K, atmospheric pressure), particles below ~60 µm fall in the very difficult to fluidize class C (cohesive), and therefore should not be considered for our process despite the apparent "functioning" calculated velocity range.

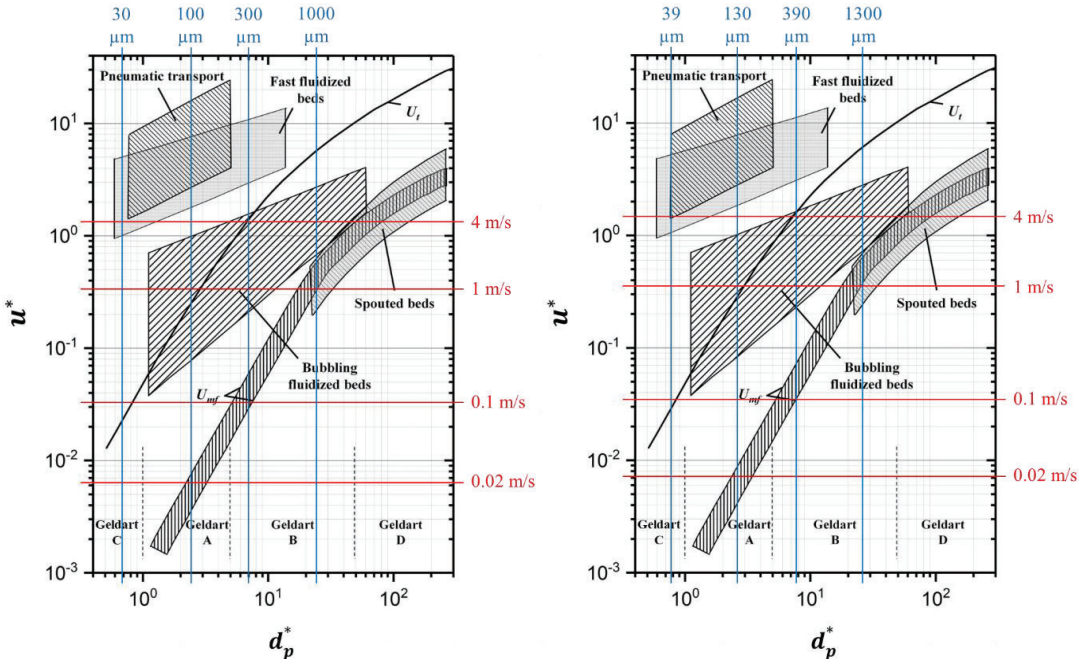

Figure 4: Diagram of fluidization regimes reproduced from Kunii and Levenspiel (2013). Additional lines correspond to specific particle diameters and fluidization velocities for iron (left) and iron oxide (right) drawn for fluidization in air at 1100 K and atmospheric pressure.

4.1.3 Combustion mechanism and power output: Surface combustion of iron particles is favored by smaller particles due to higher heat transfer rates minimizing the risk of iron vaporization. For this reason, experimental studies of iron flames usually use fine particles (Baigmohammadi et al., 2023). However, in the case of a bubbling fluidized bed process, the maximum heat generation is directly linked to the fluidizing and oxidizing gas velocity. Considering that larger particles can be fluidized at higher velocities (Geldart A and B), they also have the potential for higher heat generation. Therefore,

https://doi.org/10.52202/077185-0084

there should be a maximum iron particles size that ensures surface combustion (and thus limits nanoparticle formation) and maximizes the heat output.

4.1.4 Baseline system parameters for the numerical study: The reactor diameter was fixed at 10 cm, which was deemed a reasonable starting point for a future experimental setup. Iron particle size and superficial gas velocity was fixed to 100 µm and 0.2 m/s, prioritizing a surface combustion mechanism over heat output while ensuring satisfactory fluidization with no risk of particle entrainment. Under atmospheric pressure and a temperature of 1100 K, this corresponds to a fluidizing air mass flow rate of 1.8 kg/h. A maximum heat output of 2 kW can then theoretically be reached for stoichiometric conditions corresponding to an iron injection rate of 1 kg/h. The initial bed has a height of 3 cm and is composed exclusively of iron oxide product particles with size of 129 µm. These baseline system parameters are summarized in Table 1.

Table 1: Baseline system parameters for numerical simulations.

System parameter	Value	Unit	System parameter	Value	Unit
Reactor diameter	10	cm	Fluidizing gas mass flow rate	1.8	kg/h
Initial bed height	3	cm	Fluidizing gas superficial velocity	0.2	m/s
Fe particle size	100	µm	Fe injection rate	1	kg/h
Fe_2O_3 particle size	129	µm	Fe and N_2 injection temperature	300	K
Initial bed temperature	1100	K	Nominal heat generation	2	kW

4.2 Numerical simulations with the Eulerian multiphase model

The numerical model was set up using the commercial software ANSYS Fluent. In addition to the baseline parameters defined in Table 1, a single overbed, circular, iron injection inlet was included (see Figure 2) and the entraining nitrogen mass flow rate was fixed at 0.18 kg/h or 1/10th of the fluidizing gas flow rate. Both iron particles and the entraining nitrogen flow are injected at 300 K and at a 45° angle. The reactor height was kept at a minimum (12 cm) and the outlet diameter was reduced to 3 cm to prevent gas recirculation at the outlet.

4.2.1 Inert Fe_2O_3 fluidization at 1100 K and mesh comparison: Mesh refinement can have a significant impact on the results of multiphasic flows (Cloete & Amini, 2016; Sande & Ray, 2014). A mesh dependency analysis was performed for simulations of a fluidized oxide bed with no iron injection. Three different meshes were tested with element sizes of 1, 2 and 4 mm in the regions of interest (bottom half of the reactor and around the solid inlet) for total cell counts of 56 000, 190 000 and 1 360 000, respectively. Figure 5 shows instantaneous snapshots of oxide volume fraction, revealing the expansion of the bed and the bubble structures across the axial plane.

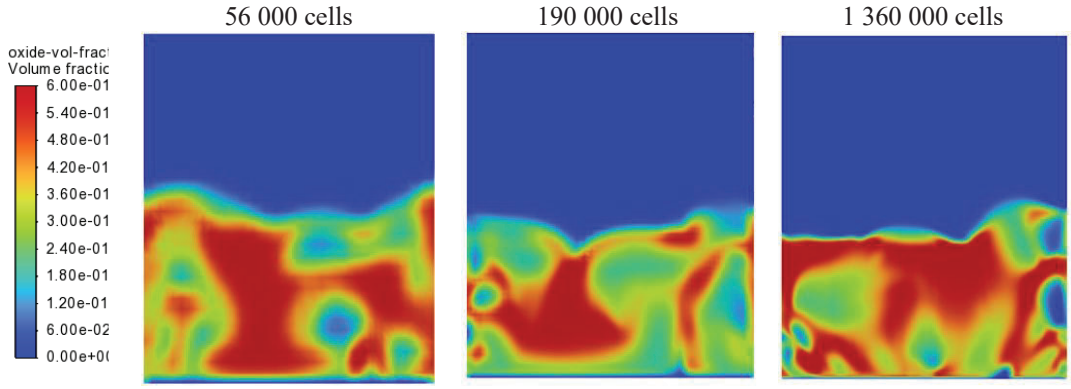

Figure 5: Snapshots of oxide volume fraction across axial plane for different mesh refinement levels.

https://doi.org/10.52202/077185-0084

As expected, the finer the mesh, the smaller the minimum size of bubble that is captured by the model. This is especially significant near the walls and at the bottom of the reactor, where only the finest mesh is able to capture the nascent bubbles. The bubbles are also "sharper", with a larger difference in volume fraction when compared to the rest of the bed. Despite that, even the coarsest mesh was able to satisfactorily capture the bed expansion and solid mixing, in line with expectations stemming from previous analytical predictions. To complement this mesh comparison, volume fraction data was recorded over approximately 1 second of calculation time for the two coarser meshes to retrieve time-averaged statistics. Time-averaged oxide volume fraction and RMSE values of gas volume fraction were averaged over different cross-sections along the reactor (Figure 6). The RMSE of gas volume fraction, particularly, characterizes the variation of the space occupied by the bubbles over the entire calculation time, and well illustrates the bubble intensity and the mixing it induces.
No time statistics are available for the finest mesh due to prohibitive calculation time.

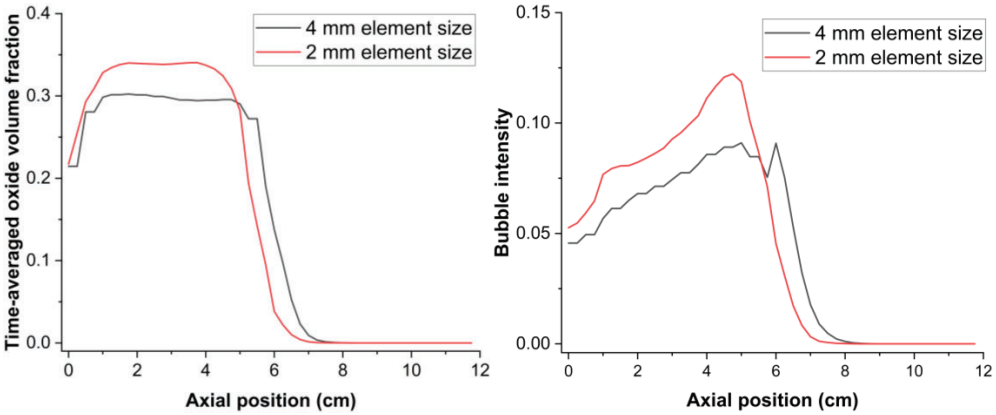

Figure 6: Time-averaged oxide volume fraction (left) and RMSE values of air volume fraction (or bubble intensity, right) along the bed for the 56000-element (in blue) and 190000-element (in red) meshes.

The time-average values of oxide volume fraction show the extend of the bed expansion for the two meshes. It appears that the finer mesh predicts a slightly denser, less expanded bed. Bubble intensity is also higher for the finer mesh, confirming the visual impressions provided by the snapshots in Figure 5. For both meshes, bubble intensity rises along the bed and reaches its maximum near the surface. This is due to the gradual coalescing and increase in size of the bubbles as they rise. The fact that no plateau is reached suggests that the bubbles could grow further in a deeper bed. Considering that in the present case, the size of bubbles reaches approximately one third of the reactor diameter as they breach the bed surface, there is a high risk of slugging flow occurring in a deeper bed with the same diameter. Overall, the general flow behavior seems to be captured even by the coarsest mesh, despite the lesser accuracy and rougher curves. The higher accuracy of the 190000-cells mesh was chosen for the first combustion simulations, but the significant reduction in calculation time provided by the 5²6000-cell mesh will be useful for analyzing the impact of different parameters.
In addition to the mesh comparison, inert fluidizing simulations have also confirmed what was speculated following the analytical assessment: indeed, when a small fraction of iron particles were included in the bed (4% of total bed mass), a rapid mixing and homogeneous distribution of those particles was observed, with no phase separation between oxide and iron. This further affirms the suitability of an iron/iron oxide bed composition.

4.2.2 Continuous over-bed iron injection and combustion: A simulation of iron particle combustion was performed for the baseline conditions defined in Table 1 and using the 190000-cells mesh. After the start of the injection, the combusting flow rapidly stabilizes after the stream of iron particles reaches the bed surface. Figure 7 presents instantaneous snapshots of oxide and iron volume fractions, oxygen mass fraction in the gas phase and heat of reaction, taken after flow stabilization. The first stage of the

https://doi.org/10.52202/077185-0084

simulation has gone as expected: iron particles, initially entrained in pure nitrogen, get mixed with oxygen and heated up. The ignition temperature is reached upon contact with the oxide bed surface, resulting in the combustion reaction. However, considering that the overall mixture is stoichiometric, the stabilized flow/combustion appears to be inaccurate. Indeed, despite a clear oxygen consumption zone around the reacting iron (Figure 7 c), a large portion of the oxygen flow remains untouched and flows out of the reactor, whereas almost all of the iron is consumed by the reaction.

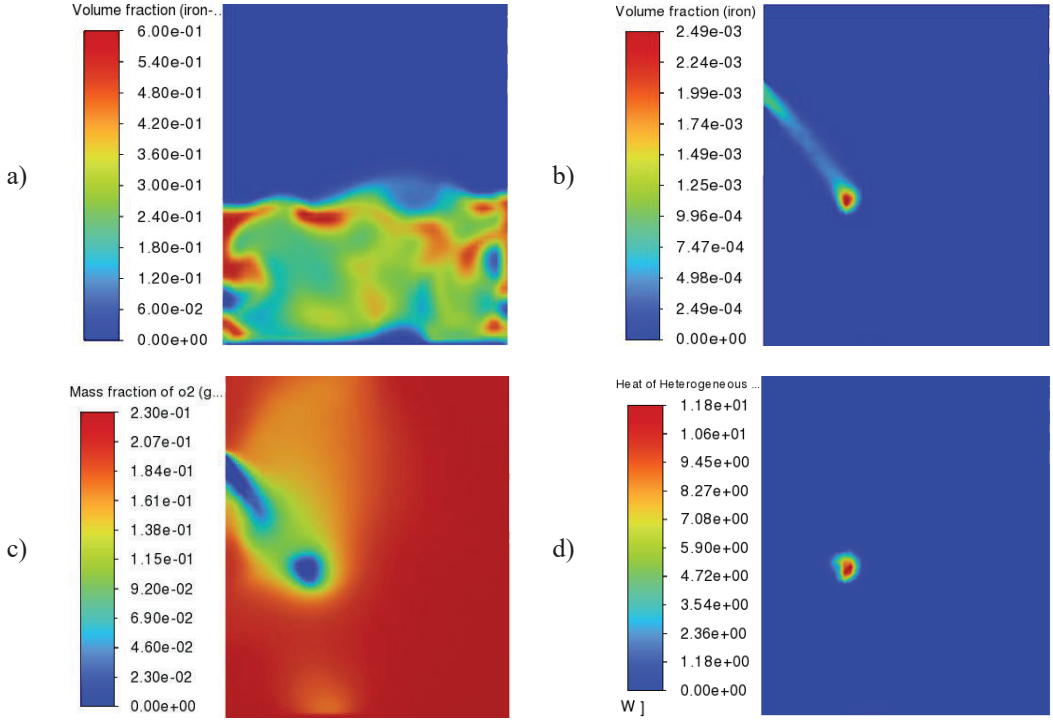

Figure 7: Snapshots of a) Oxide volume fraction – b) Iron volume fraction c) Oxygen mass fraction in the gas phase – d) Heat of reaction.

This suggests important inaccuracies in the species balance. To quantify this, the mass of iron and oxygen consumed by the reaction was defined as follows:

$$\dot{m}^{Fe}_{Reacted} = \frac{m^{Fe}_{t2} - m^{Fe}_{t1}}{t_2 - t_1} - \dot{m}^{Fe}_{inlet} \tag{12}$$

$$\dot{m}^{O_2}_{Reacted} = \frac{m^{O_2}_{t2} - m^{O_2}_{t1}}{t_2 - t_1} - \dot{m}^{O_2}_{inlet} - \dot{m}^{O_2}_{outlet} \tag{13}$$

These parameters were monitored over the entire calculation. For easier comparison, $\dot{m}^{O_2}_{Reacted}(from\ Fe\ balance)$ was defined as follows, with $R_{stoich} = 0.42$ the theoretical ratio between oxygen and iron stoichiometric consumption rates:

$$\dot{m}^{O_2}_{Reacted}(from\ Fe\ balance) = R_{stoich} * \dot{m}^{Fe}_{Reacted} \tag{14}$$

Similarly, the total heat output Q_{tot} was compared with the heat output corresponding to the reacted mass of iron multiplied by its energy density ED^{Fe}:

$$Q_{tot}(from\ Fe\ balance) = -ED^{Fe} * \dot{m}^{Fe}_{Reacted} \tag{15}$$

Figure 8 shows the difference between the mass of reacted oxygen directly retrieved from the simulation, and the expected oxygen consumption based on the mass of reacted iron. A similar comparison is also shown for the generated heat. The figure confirms what was already qualitatively visible on the snapshots in Figure 7: after the stabilized state is reached, there is an important discrepancy between reaction rate of iron and that of oxygen. After stabilization, the iron reaction rate

https://doi.org/10.52202/077185-0084

is very close to its injection rate; however, the oxygen consumed in the domain should only allow for around 30% of that reaction rate. Such an important error significantly limits the potential of the model for assessing the impact of different flow parameters on the process' behavior. Thus, it is important to assess the possible reasons for such inaccuracies to correct the model.

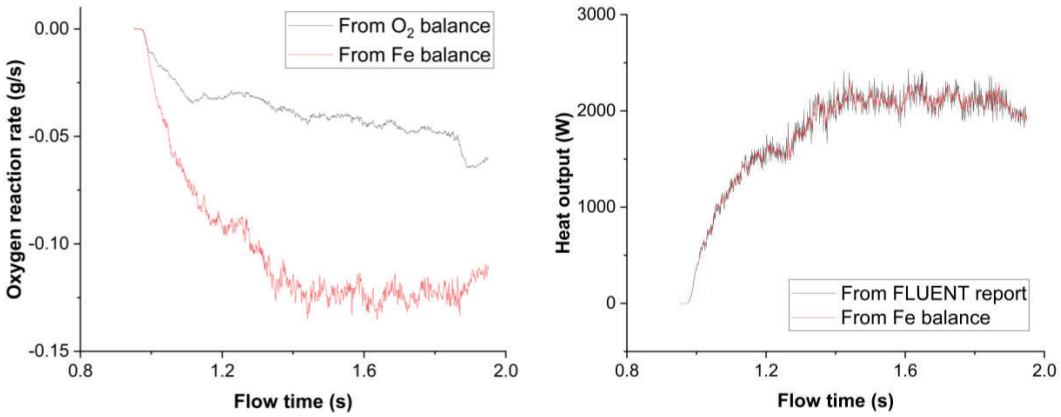

Figure 8: Difference between $\dot{m}^{O_2}_{Reacted}$ and $\dot{m}^{O_2}_{Reacted}(from\ Fe\ balance)$(left) and between Q_{tot} and $Q_{tot}(from\ Fe\ balance)$ (right) from the start of iron injection to flow stabilization.

The heat generation (as well as the oxide mass balance, not displayed here) in the domain appear to closely match the iron consumption rate instead of that of oxygen. This could suggest that the main source of error is found in the oxygen species balance calculation. However, when considering the overall flow behavior, it is actually the opposite. Indeed, in the present case, the concentrated stream of iron particles is expected to enter the fluidized bed and begin to react. But considering the global stoichiometric conditions and the fast reaction rate, a local oxygen deficit is expected to form at the point where the iron stream enters the bed. The expected outcome would then be a progressive diffusion of unreacted iron particles in the entire bed, leading to relatively homogeneous conditions. In the present simulation however, iron is consumed rapidly and entirely, and the reaction is thus limited to a small region of the bed. In these conditions, the present oxygen consumption is coherent with the general flow: a small fraction of the oxygen is consumed in the reduced reaction zone, while most of the oxygen flows past with no iron to react with. From this perspective, the "origin" of the simulation inaccuracies would be an iron species imbalance, with the error propagating to the other aspects of the simulation (oxide formation, energy release and oxygen flow and consumption).

5 CONCLUSIONS

- An analytical approach was used to propose baseline system parameters for a fluidized bed iron combustion process. The proposed small-scale system is suitable for 2 kW heat output and can be easily matched with experimental means.
- The proposed small-scale system was simulated in Fluent following the Eulerian multiphase approach which is extensively used for similar processes. The simulation of the inert fluidized bed was satisfactory. Even a relatively coarse mesh was deemed sufficient to capture the main flow structures and allow for advanced parametric analysis in future works.
- A simplistic reaction mechanism was implemented to model the combustion of iron. Although part of the involved phenomena was coherent with expectations, a significant discrepancy between oxygen and iron consumption rates was observed, leading to a globally inaccurate flow. Although the exact source of the error is uncertain, it seems to be closely linked to the species balance calculation. The use of an open-source software, or User Defined Functions within Fluent, might be necessary to achieve better control over the mass source terms during the calculation and ensure the stoichiometry of the reaction. Another aspect to improve is the formulation of the reaction rate (Equation 11), as its rough simplification could be the reason for the observed numerical error.

https://doi.org/10.52202/077185-0084

NOMENCLATURE

u_{mf}	minimum fluidization velocity	(m/s)
u_t	terminal velocity	(m.s^{-1})
d	diameter	(m)
ρ	density	(–)
ρ_{rq}	phase reference density	(kg. m^{-3}.s^{-1})
μ	dynamic viscosity	(kg.m^{-1}.s^{-1})
g	earth gravitational acceleration	(m.s^{-2})
α	volume fraction	(–)
$\vec{v}$	velocity vector	(m/s)
$\dot{m}$	mass flow rate	(kg.s^{-1})
$\dot{m}_{pq}$	mass transfer between phases p and q	(kg. m^{-3}.s^{-1})
p	pressure	(Pa)
$\bar{\bar{\tau}}$	stress-strain tensor	(Pa)
K	interphase momentum exchange coefficient	(kg.m^{-3}.s^{-1})
$\vec{v}$	velocity vector	(m.s^{-1})
$\vec{F}_{td}$	turbulent dispersion force	(kg.m.s^{-2})
e	internal energy	(J)
h	enthalpy	(J)
k	conductivity	(m.K^{-1}.s^{-3})
T	temperature	K
$\vec{J}$	diffusive flux of species	(kg.J^{-1}.s^{-3})
Q_{pq}	intensity of heat exchange between phases	(J.m^{-3}s^{-1})
S	source term	(kg.m^{-1}.s^{-3})
Y	mass fraction	(–)
R	reaction rate	(kmol.m^{-3}.s^{-1})
t	time	(s)
M	molar mass	(kg.kmol^{-1})
A	pre-exponential constant	(s^{-1})
ED	energy density	(J.kg^{-1})
R_{stoich}	mass consumption ratio between oxygen and iron at stoichiometry (–)	

Subscript

s	solid particle
g	gas
q, p	relative to phase q and/or p
i	species i
eff	effective
Fe, O_2	iron, oxygen

REFERENCES

Allanore, A., Ortiz, L. A., & Sadoway, D. R. (2011). Molten Oxide Electrolysis for Iron Production: Identification of Key Process Parameters for Largescale Development. *Energy Technology 2011: Carbon Dioxide and Other Greenhouse Gas Reduction Metallurgy and Waste Heat Recovery*, 121–129. https://doi.org/10.1002/9781118061886.CH12

Ansys Fluent Theory Guide. (2023). http://www.ansys.com

Baigmohammadi, M., Prasidha, W., Stevens, N. C., Shoshyn, Y. L., Spee, T., & de Goey, P. (2023). Towards utilization of iron powders for heating and power. *Applications in Energy and Combustion Science*, *13*, 100116. https://doi.org/10.1016/J.JAECS.2023.100116

https://doi.org/10.52202/077185-0084

Bergthorson, J. M. (2018). Recyclable metal fuels for clean and compact zero-carbon power. *Progress in Energy and Combustion Science*, *68*, 169–196. https://doi.org/10.1016/j.pecs.2018.05.001

Bergthorson, J. M., Goroshin, S., Soo, M. J., Julien, P., Palecka, J., Frost, D. L., & Jarvis, D. J. (2015). Direct combustion of recyclable metal fuels for zero-carbon heat and power. *Applied Energy*, *160*, 368–382. https://doi.org/10.1016/j.apenergy.2015.09.037

Bhaskar, A., Assadi, M., & Somehsaraei, H. N. (2020). Decarbonization of the iron and steel industry with direct reduction of iron ore with green hydrogen. *Energies*, *13*(3).

Cloete, S., & Amini, S. (2016). The dense discrete phase model for simulation of bubbling fluidized beds: Validation and verification. *9th International Conference on Multiphase Flow* .

Fedoryk, M., Stelzner, B., Harth, S., & Trimis, D. (2023). Experimental investigation of the laminar burning velocity of iron-air flames in a tube burner. *Applications in Energy and Combustion Science*, *13*, 100111. https://doi.org/10.1016/J.JAECS.2022.100111

Gidaspow, D., Bezburuah, R., & Ding, J. (1991). Hydrodynamics of circulating fluidized beds: Kinetic theory approach. *7th International Conference on Fluidization*.

Guío-Pérez, D. C., Martinez Castilla, G., Pallarès, D., Thunman, H., & Johnsson, F. (2023). Thermochemical Energy Storage with Integrated District Heat Production–A Case Study of Sweden. *Energies*, *16*(3), 1155. https://doi.org/10.3390/EN16031155/S1

Janicka, J., Debiagi, P., Scholtissek, A., Dreizler, A., Epple, B., Pawellek, R., Maltsev, A., & Hasse, C. (2023). The potential of retrofitting existing coal power plants: A case study for operation with green iron. *Applied Energy*, *339*, 120950. https://doi.org/10.1016/J.APENERGY.2023.120950

Julien, P., & Bergthorson, J. M. (2017). Enabling the metal fuel economy: Green recycling of metal fuels. *Sustainable Energy and Fuels*, *1*(3), 615–625. https://doi.org/10.1039/c7se00004a

Kunii, D., & Levenspiel, O. (2013). *Fluidization Engineering* (Second Edition).

Mi, X., Fujinawa, A., & Bergthorson, J. M. (2022). A quantitative analysis of the ignition characteristics of fine iron particles. *Combustion and Flame*, *240*, 112011.

Mich, J., Braig, D., Gustmann, T., Hasse, C., & Scholtissek, A. (2023). A comparison of mechanistic models for the combustion of iron microparticles and their application to polydisperse iron-air suspensions. *Combustion and Flame*, *256*, 112949.

Ning, D., Shoshin, Y., van Oijen, J. A., Finotello, G., & de Goey, L. P. H. (2021). Burn time and combustion regime of laser-ignited single iron particle. *Combustion and Flame*, *230*.

Ning, D., Shoshin, Y., van Oijen, J. A., Finotello, G., & de Goey, L. P. H. (2022). Critical temperature for nanoparticle cloud formation during combustion of single micron-sized iron particle. *Combustion and Flame*, *244*, 112296. https://doi.org/10.1016/j.combustflame.2022.112296

Sande, P. C., & Ray, S. (2014). Mesh size effect on CFD simulation of gas-fluidized Geldart A particles. *Powder Technology*, *264*, 43–53. https://doi.org/10.1016/J.POWTEC.2014.05.019

Sarkar, D. K. (2015). Fluidized-Bed Combustion Boilers. In *Thermal Power Plant* (pp. 159–187). Elsevier. https://doi.org/10.1016/b978-0-12-801575-9.00005-6

Sun, J.-H., Dobashi, R., & Hirano, T. (n.d.). *Combustion Behavior of Iron Particles Suspended in Air*.

Tang, F. D., Goroshin, S., & Higgins, A. J. (2011). Modes of particle combustion in iron dust flames. *Proceedings of the Combustion Institute*, *33*(2), 1975–1982.

Thijs, L. C., van Gool, C. E. A. G., Ramaekers, W. J. S., van Oijen, J. A., & de Goey, L. P. H. (2022). Resolved simulations of single iron particle combustion and the release of nano-particles. *Proceedings of the Combustion Institute*, S1540748922000682.

Vecchi, A., Knobloch, K., Liang, T., Kildahl, H., Sciacovelli, A., Engelbrecht, K., Li, Y., & Ding, Y. (2022). Carnot Battery development: A review on system performance, applications and commercial state-of-the-art. *Journal of Energy Storage*, *55*, 105782.

Vecchi, A., & Sciacovelli, A. (2023). Long-duration thermo-mechanical energy storage – Present and future techno-economic competitiveness. *Applied Energy*, *334*, 120628.

ACKNOWLEDGEMENT

The Authors would like to acknowledge the financial support from the UK Engineering and Physical Science Research Council (EPSRC) for the project ‘MIX-MOXes’ (EP/X000249/1).

 https://doi.org/10.52202/077185-0084